Chapter 05

A dislocation density reliant mean-field model to describe the creep response and microstructure evolution of superalloy IN-718

Abstract: Inconel®718 alloy presents high creep resistance and its creep response depends on the stress, temperature and the microstructural ingredients. The mesoscale creep models developed in the literature usually do not consider the microstructure evolution. Therefore, a physically-based creep model is presented that considers the amount and size of strengthening precipitates. The internal variables of the model are the densities of mobile and immobile dislocations, and the mean free path. The developed model addresses the primary and secondary regime of creep and reproduces the creep curves that resemble the experimental ones, along with the evolution of internal variables. Additionally, model outputs are validated using electron backscattered diffraction (EBSD) investigations. It was shown that the immobile dislocation density has the same order of magnitude as the estimated boundary dislocation density from the EBSD analysis. Furthermore, the model suggests that both the dislocation densities, internal stress and climb stress increase over the period of creep. In contrast, the mean free path, glide velocity and effective stress have a decreasing trend.

5.1. Introduction

Inconel®718 (IN-718) superalloy presents excellent mechanical properties and oxidation resistance at elevated temperatures (T) and is an ideal candidate for manufacturing the hot sections of powerplants and aero engines. The precipitates such as γ'-$Ni_3(Al, Ti)$-$(L1_2)$ and γ''-Ni_3Nb-($D0_{22}$) play a crucial role in providing mechanical strength at high-temperature over time. The γ'' phase

is more effective for strengthening compared to the γ' phase [2, 6]. Additionally, the δ- Ni_3Nb-($D0_a$) precipitates restrict the grain boundary migration during different exposure conditions [1, 6, 56, 202-205] . Furthermore, a material exposed to creep will experience microstructural modifications such as the annihilation, formation and rearrangement of dislocations and nucleation, growth, coarsening and dissolution of precipitates. Undesired cavitation will additionally lead to failure. The synergistic effect of the aforementioned mechanisms results in the accumulations of plastic creep strain that is observed during failure and measured/reported/modelled by different researchers [154, 206-208]. The creep modelling combined with characterization methods such as X-ray diffraction (XRD), Transmission electron microscope (TEM) and EBSD can address the property deterioration and enable tracking of microstructure evolution with creep time to prevent failure or design new creep-resistant alloys.

Over the last decades, several empirical models have been developed to estimate the creep strain with respect to time by capturing the influence of applied stress and T [8, 14, 43, 53, 61, 157, 196, 209-213].These models address the creep curves nicely but provide little information about the deformation mechanisms and microstructure evolution with ongoing creep. The deformation mechanism of the metallic materials at the elevated T is inherently associated with its stacking fault energy (SFE) [214]. In general, a low SFE material such as some Ni-based super alloys or 304HCu steel usually undergoes a complex microstructure evolution during the deformation at elevated temperatures that includes coarsening of precipitates and dislocation hardening [41, 62, 215]. For high SFE materials, perfect dislocations form, annihilate and re-arrange forming subgrains as shown in materials like RAFM steel [216] and 9 % Cr martensitic steels [57, 58, 212, 215, 217, 218]. The aforementioned empirical models also do not include the influence of SFE on creep and need to be explored.

On the other side, we find physics knowledge-based models that consider the evolution of microstructural features during the plastic deformation of the materials, either in creep conditions [47, 53, 58] or at constant strain rates [78, 113]. The microstructure may consist of different dislocation densities, subgrain radius, precipitate number density and mean radius. These creep models can establish the relation between the microstructure variation and creep rate. Most of the models account for dislocations that climb and glide. Dyson's [53] model considers that obstacles like precipitates, dislocations and grain boundaries hinder the dislocations' motion in Nimonic superalloy. Following a similar microstructure-reliant concept, Manonukul et al. [219] modelled the creep performance of a Ni-based superalloy considering the pinning of dislocations at the precipitates, and Kim et al. [56]estimated the total creep due to grain boundary sliding. A recent model from Wu et al. [62] adopts the dislocation glide concept from Dyson [53] and a combination of the dislocation motion, grain boundary sliding, and cavitation phenomena to capture the creep rate of additively manufactured nickel-based superalloys, i.e., IN-718 and IN738LC. Few other microstructure-reliant creep models were developed in the past [55, 159, 215] and validated with creep curves of steels or Ni-based 617 superalloy.

These models [49, 55] either do not provide information about the microstructural changes occurring during creep or employ too many adjustable parameters [58, 215]. Thus, a sound model that considers the influence of SFE on creep, explains the evolution of the internal variable along with creep curves, and works with a single set of calibration parameters, especially in the case of nickel-based superalloys is a need.

This chapter mainly deals with developing a physical-based creep model to address the primary and secondary creep regimes of an IN-718 superalloy. The work also incorporated the influence of the SFE on the glide and climb motion of the dislocations into the model. We validated the

model using the creep curves obtained from uniaxial tensile creep testing at different T and σ conditions and the microstructural features from EBSD measurements. Finally, we could determine the evolution of the mobile dislocation density, immobile dislocation density, mean free path and other important variables.

5.2. Experimental

5.2.1. *Material and uniaxial tensile creep testing*

The composition of Inconel®718 investigated herein, is given Table 5.1. The material was received after forging followed by direct aging (DA). Heat treatment involves aging at 720 °C for 8 hours, then cooling to 620 °C and holding for 8 h followed by air cooling. The tensile creep specimens were machined with length = 90 mm and diameter = 6.5 mm following a DIN EN ISO 204 M16 standard. The creep testing was carried out employing the ASTM E139 at three different temperatures and loads. The creep tests were conducted at constant load with the help of machine Mayes model mark II TC. The uniaxial tensile creep testing of the IN-718 superalloy has been conducted at 593 ℃ / 552 MPa, 593 ℃ / 662 MPa, 593 ℃ / 827 MPa, 620 ℃ / 552 MPa, 620 ℃ / 662 MPa, 620 ℃ / 827 MPa, 650 ℃ / 552 MPa and 650 ℃ / 662 MPa.

Table 5.1. Details of Inconel®718 in terms of alloying elements

Elements	**Ni**	**Cr**	**Fe**	**Mo**	**Al**	**Co**	**Si**	**Nb**	**C**	**Mn**	**Ti**
wt.%	Bal.	17.920	17.180	2.990	0.560	0.270	0.070	5.420	0.021	0.080	1.020

5.2.2. *Microstructure characterization*

We analyzed the microstructure of the as-received and gauge parts of the crept samples using the EBSD technique. Therefore, we mounted the samples, ground them with SiC paper, and polished them with colloidal silica suspension (OP-S). EBSD measurements were performed using a Hikari

detector and the TSL-OIM software equipped with TESCAN Mira3 scanning electron microscope. The measurement was performed on the area of 350 × 350 μm^2, with a step size of 500 nm. Inverse Pole Figure (IPF) and Kernel Average Misorientation (KAM) maps were generated accordingly. We investigated the boundary dislocation density employing a well-established method reported in the literature [98, 99, 220]. It has to be mentioned that area with the sign of recrystallization were not included in the dislocation density estimation.

5.3. Model formulation

The model to describe creep consists of three main components: the microstructure conceptualization, mechanisms of microstructural changes, rate and the constitutive equations. The proposed dislocation mean-field model for IN-718 has been developed based on the research conducted by different researchers [47, 57, 58, 62, 158, 221]. With respect to these previously developed creep models, the advancement in this work includes, generalized 1. rate equations that include the number of active slip systems 2. mean free path consisting of all possible obstacles 3. glide velocity model that is more realistic in terms of SFE and effective stress 4. climb velocity model that incorporate the stacking fault factor dependency 5. single set of parameters for modelling the creep response and microstructure evolution.

5.3.1. *Microstructure conceptualization*

Figure 5.1 shows the schematic microstructure of the received IN-718 superalloy. The microstructure consists of the high-angle grain boundary, the precipitates γ'-$Ni_3(Al,Ti)$-$(L1_2)$ and γ''-Ni_3Nb-$(D0_{22})$ and different dislocation configurations. The related internal variables for precipitates are the volume fraction and mean radius, and for dislocations, they are their corresponding densities. The dislocations are categorized into two groups: the mobile dislocations, free to glide and responsible for the plastic strain, and the immobile dislocations. The mechanisms

that alter the properties during creep are the dislocation production and the dislocation annihilation and rearrangement, change in precipitation state (nucleation, growth, coarsening and dissolution) and cavitation. Our model does not consider the cavitation process as the tertiary creep is not targeted in this study.

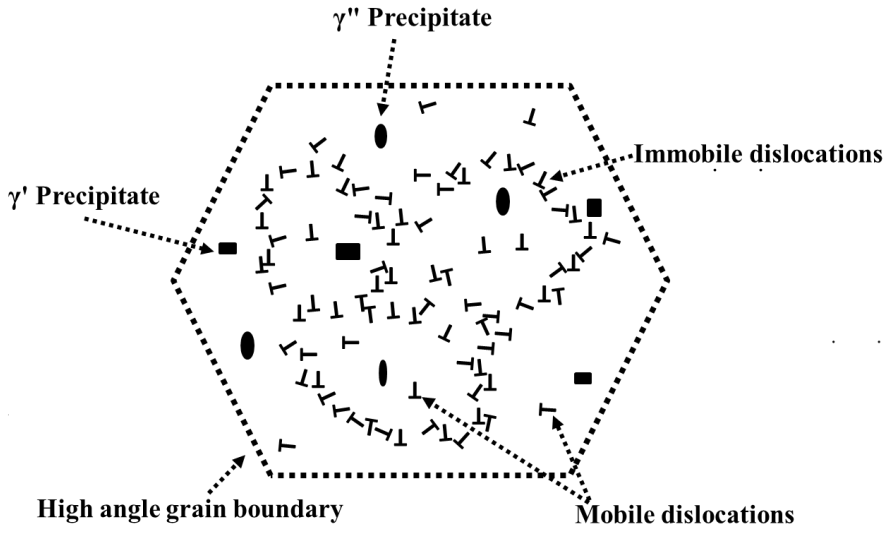

Figure 5.1. Representative microstructure of as received IN-718 superalloy considered in the model

The plastic strain accumulates up to the secondary creep stage primarily due to the movement of dislocations. The creep-related phenomena are the hardening due to dislocation production by Frank-Read (F-R) sources and the recovery due to dislocation annihilation and rearrangement. The evolution of mobile dislocation density during creep can be expressed by Equation (5.1) as a combination of production and recovery/annihilation terms.

$$\dot{\rho}_m = \overbrace{\underbrace{\left(\frac{v_{gl}}{\lambda_{mean}}\rho_m\right)}_{production}}^{\rho_m^+} - \overbrace{\underbrace{\left(\frac{v_{gl}}{s}\rho_m\right)\left(1-\frac{1}{n_{slip}}\right)}_{immoblization} - \underbrace{d_{spon}\rho_m v_{gl}(\rho_m+\rho_i)\left(\frac{1}{n_{slip}}\right)}_{glide\ recovery}}^{\rho_m^-}, \tag{5.1}$$

In Equation (5.1), n_{slip} is the number of active glide systems and $s = k_c/(\rho_i)^{0.5}$ is the dislocation substructure size, where k_c is the calibration parameter. Herein, we only considered the active glide systems. We assumed that the total number of active glide systems is $n_{slip,}$ and an equal number of dislocations are available on each system. The normalisation will be $1/n_{slip}$, for any dislocation reaction. Furthermore, since the reaction partners are available on all glide systems, we replaced $1/n_{slip}$ with $(n_{slip}-1)/n_{slip}$ [113].

The newly formed mobile dislocations can interact with obstacles, precipitates or substructure walls, and become immobile. Similar to mobile dislocations, we describe the evolution of ρ_i during creep by the differential Equation (5.2) that considers one production and two reduction terms.

$$\dot{\rho}_i = \overbrace{\underbrace{\left(\frac{v_{gl}}{s}\rho_m\right)\left(1-\frac{1}{n_{slip}}\right)}_{immoblization}}^{\rho_i^+} - \overbrace{\underbrace{k\frac{v_{cl}}{h_i}\rho_i\left(\frac{1}{n_{slip}}\right)}_{climb\ recovery} - \underbrace{d_{spon}(\rho_m\rho_i v_{gl})\left(\frac{1}{n_{slip}}\right)}_{glide\ recovery}}^{\rho_i^-} \tag{5.2}$$

5.3.2. *Precipitates and other obstacles*

Frank-Read sources operate with a frequency v_{gl}/λ_{mean}. We considered that the mean free path λ_{mean} must represent the geometric mean of average obstacle distance for all different possibilities. Figure 5.2 illustrates the different obstacles a mobile dislocation may encounter during travel. Therefore, we can use Equation (5.3) to calculate $\lambda_{mean,}$ accounting for the mean mobile dislocation spacing h_m, the mean distance between gamma prime precipitate $L_{p,\gamma'}$, the mean distance between gamma double prime precipitate $L_{p,\gamma''}$, and the average substructure size s, [113, 139].

$$\frac{1}{\lambda_{mean}} = \frac{\beta_{h_m}}{h_m} + \frac{\beta_s}{s} + \frac{\beta_{L_{p,\gamma'}}}{L_{p,\gamma'}} + \frac{\beta_{L_{p,\gamma''}}}{L_{p,\gamma''}}, \tag{5.3}$$

where β_{h_m}, β_s , $\beta_{L_{p,\gamma'}}$ and $\beta_{L_{p,\gamma''}}$ are the calibration parameters.

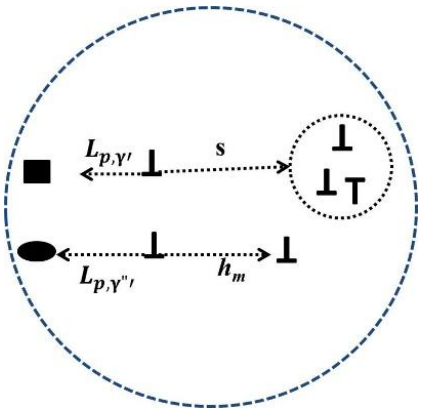

Figure 5.2. Schematic diagram illustrating the different obstacles a mobile dislocation may encounter during the travel

In Equation (5.3), the average distance between the precipitates $L_{p,i}$ of type ith precipitates is given by Equation (5.4) as [113],

$$L_{p,i} = \frac{r_{p,i}}{\sqrt{v_{p,i}}}, \tag{5.4}$$

In Equation (5.4), $r_{p,i}$ represents the mean radius of precipitates, $v_{p,i} = 4/3\pi r_{p,i}^3 N_{v,i}$ is the phase fraction of the precipitates and $N_{v,i}$ represents the number density of precipitates. The coarsening of the precipitates occurs due to the Ostwald ripening mechanism and leads to increase the $L_{p,i}$ and hence alters the overall mean free path during creep. Equation (5.5) represents the coarsening behaviour of precipitates as,

$$r_{pi}^n - r_{i0}^n = k_{d_i} t \tag{5.5}$$

According to the published reports [222, 223] the measured coarsening kinetics of the γ'' precipitate in the IN-718 superalloy is linearly related to the cube root of the aging time. Therefore, herein, *n* equals 3 for both types of precipitates. By differentiating the Ostwald ripening equation, we determine the precipitate coarsening rate as,

$$\dot{r}_{p_i} = \frac{k_{d_i}}{n.r_{p_i}^{(n-1)}}, \tag{5.6}$$

The coarsening constant k_{d_i}, given in Appendix 5.B, controls the coarsening kinetics of the precipitates and *i=1, 2* denotes γ' and γ'' precipitates, respectively.

5.3.3. *Constitutive equations: internal and effective stresses and creep strain*

Not all the stress applied to a material σ_{appl} at elevated temperature *T* results in the glide of dislocations. Some part of the applied stress has to overcome the resistance of the microstructure. This part of the applied stress is called internal stress σ_{int}, and some works proposed different approaches to estimate it. Argon and Takeuchi [158] consider that the internal stress results from the interaction of mobile dislocation. Additionally, Ghoniem et al. [47] and Salazar et al. [170] included the effect of the precipitates and dislocation dipoles. Basirat et al. [55] and Yadav et al. [58] included Taylor's hardening by mobile and dipole dislocations. In the current research work, we calculated σ_{int} using Equation (5.7), as being dependent on mobile and immobile dislocations.

$$\sigma_{int} = \alpha M G_T b \sqrt{\rho_m + w_i \,.\, \rho_i} \tag{5.7}$$

We used a weight factor w_i to unify the different stress fields of the mobile and immobile dislocations under a single dislocation interaction parameter α. It is known that the stress field around mobile dislocation is higher than that of immobile dislocations. Finally, we calculated the available effective stress that is exerted on dislocations and is responsible for their movement using Equation (5.8),

$$\sigma_{effe} = \sigma_{appl} - \sigma_{int}, \tag{5.8}$$

We calculated the accumulated plastic strain during creep using the fundamental Orowan Equation [48] to reproduce the creep curve as,

$$\dot{\varepsilon} = \frac{\rho_m b v_{gl}}{M} \tag{5.9}$$

5.3.4. *Glide velocity, climb velocity and climb stress and the influence of SFE*

Ghoniem et al. [47] used the model to estimate the v_{gl} of dislocations as a function of the effective stress and temperature. In contrast, Dyson [53] and Wu et al. [62] proposed a model for v_{gl} as a function of the σ_{effe} and precipitate spacing. Furthermore, Tian et al. [224, 225] reported that increasing the stacking fault energy (SFE) values increases the creep rate due to enhanced dislocation recovery. Argon and Takeuchi [158] developed a model to estimate the v_{gl} of dislocations considering the influence of the SFE. Thus, by combining the influence of SFE, effective stress, temperature and mean spacing of precipitates, the equation for v_{gl} can be represented as,

$$v_{gl} = a_1 M \Gamma \left(\frac{1}{b r_p}\right) v_p L_p C_j D_s \sinh\left(\frac{\sigma_{effe} b^2 L_p}{M K_B T}\right), \tag{5.10}$$

In Equation (5.10), a_1 is a prefactor for the gliding velocity, $\Gamma=(X/G_T b)^2$ is the stacking fault factor, X is the magnitude of the SFE, $L_p = 1 / (L_{p,}\gamma' + L_{p,}\gamma'')$ is the mean spacing between all types of precipitates, C_j is the jog density, and D_s is the solute diffusion coefficient. See Appendix 5.A to calculate the chemical composition-dependent SFE (adapted from Tian et al. [224]). In the literature, stress that governs the movement of dislocations was considered to be the shear stress in the work of Dyson [53] and applied stress in the work of Wu et al. [62], whereas σ_{effe} is considered in this work.

Using the stacking fault factor and climb stress, we estimated the climb velocity with Equation (5.11) [1,61] as,

$$v_{cl} = \frac{\Omega D_{vp} \sigma_{cl}}{b K_B T} . \Gamma, \tag{5.11}$$

The climb stress σ_{cl} is given by Equation (5.12) [47, 78] ,

$$\sigma_{cl} = \frac{G_T b}{2\pi(1-\vartheta)\lambda_{mean}}, \tag{5.12}$$

5.4. Model set up

We employed MATLAB software and the ODE-45 solver to solve Equations (5.1–5.12). The Runge-Kutta method, included in the ODE-45 solver has good accuracy of the numerical computation. The model relies on the average values for the internal variables and related parameters. Table 5.2 summarizes the initial input values of the variables used in the model. Appendix 5.B summarizes the *T*-dependent equations for k_{d_1} and k_{d_2} for the precipitate coarsening. The materials constants and optimized parameters incorporated in the model are also summarized in Table 5.3 and Table 5.4, respectively.

Table 5.2. Input parameters for creep model of IN-718 superalloy

Microstructure inputs	**Symbol (units)**	**Value**	**Reference**
Initial mobile dislocation density	$\rho_{m0}\,(m^{-2})$	$5.13 \times 10^{12.0}$	This work
Initial immobile dislocation density	$\rho_{i0}\,(m^{-2})$	$2.43 \times 10^{14.0}$	This work
Radius of γ' precipitate	$r_{i0}(nm)$	6.930	Simulated
Radius of γ" precipitate	$r_{i0}(nm)$	8.980	Simulated
Number density γ' precipitate	$N_{v,i}(m^{-3}$	$4.760\times 10^{22.0}$	Simulated
Number density γ" precipitate	$N_{v,i}(m^{-3}$	$3.980\times 10^{22.0}$	Simulated

$$Objective\ function = \sqrt{\frac{(expeimental\ data - \ simulation\ results)}{expeimental\ data}} \tag{5.13}$$

The parameter calibration aims to reduce the differences between the experimental data and the corresponding simulated results obtained by the model. For minimizing the error, we minimized the objective function using the "Matlab fminsearch" toolbox (see equation 5.13) which is based on the Nelder-Mead simplex algorithm as elucidated in [122].

Table 5.3. Material constants used for IN-718

Parameter	**value**	**Reference**
b (m)	$2.54 \times 10^{-10.0}$	[29]
G_T (N/m^{-2})	$(-0.0323\times(T-273) + 80.1112) \times 10^{9.0}$	[124]
k_B (J/k)	$1.3806504\times 10^{-23.0}$	-
ϑ	0.31	[29]
n_{slip}	6	[226]
M	3.06	[29]

Table 5.4. Calibrated parameters incorporated in the model

$\boldsymbol{a_1}$	$\boldsymbol{\alpha}$	$\boldsymbol{d_{spon}(nm)}$	$\boldsymbol{w_i}$	$\boldsymbol{Q_{vp}(KJ/mol)}$	$\boldsymbol{Q_s(KJ/mol)}$	$\boldsymbol{\beta_{h_m}}$	$\boldsymbol{\beta_s}$	$\boldsymbol{\beta_{L_{p,\gamma'}}}$
0.68	0.49	0.807	0.423	372.45	147.16	1	0.49	1.75
$\boldsymbol{\beta_{L_{p,\gamma''}}}$	$\boldsymbol{k}$	$\boldsymbol{C_j}$	$\boldsymbol{k_c}$					
0.99	10.99	$1.51\times 10^{-6.0}$	97.11					

5.5.Results and Discussion

5.5.1. *Creep strain*

Figure 5.3 shows the experimental and simulated creep curves of the IN-718 superalloy in the temperature range of 593 ℃ - 650 ℃ and stress range of 552 MPa - 827 MPa. The simulated curves agree with the experiments till secondary stage and deviate when reaching the tertiary creep regime affected by cavitation and recrystallization.

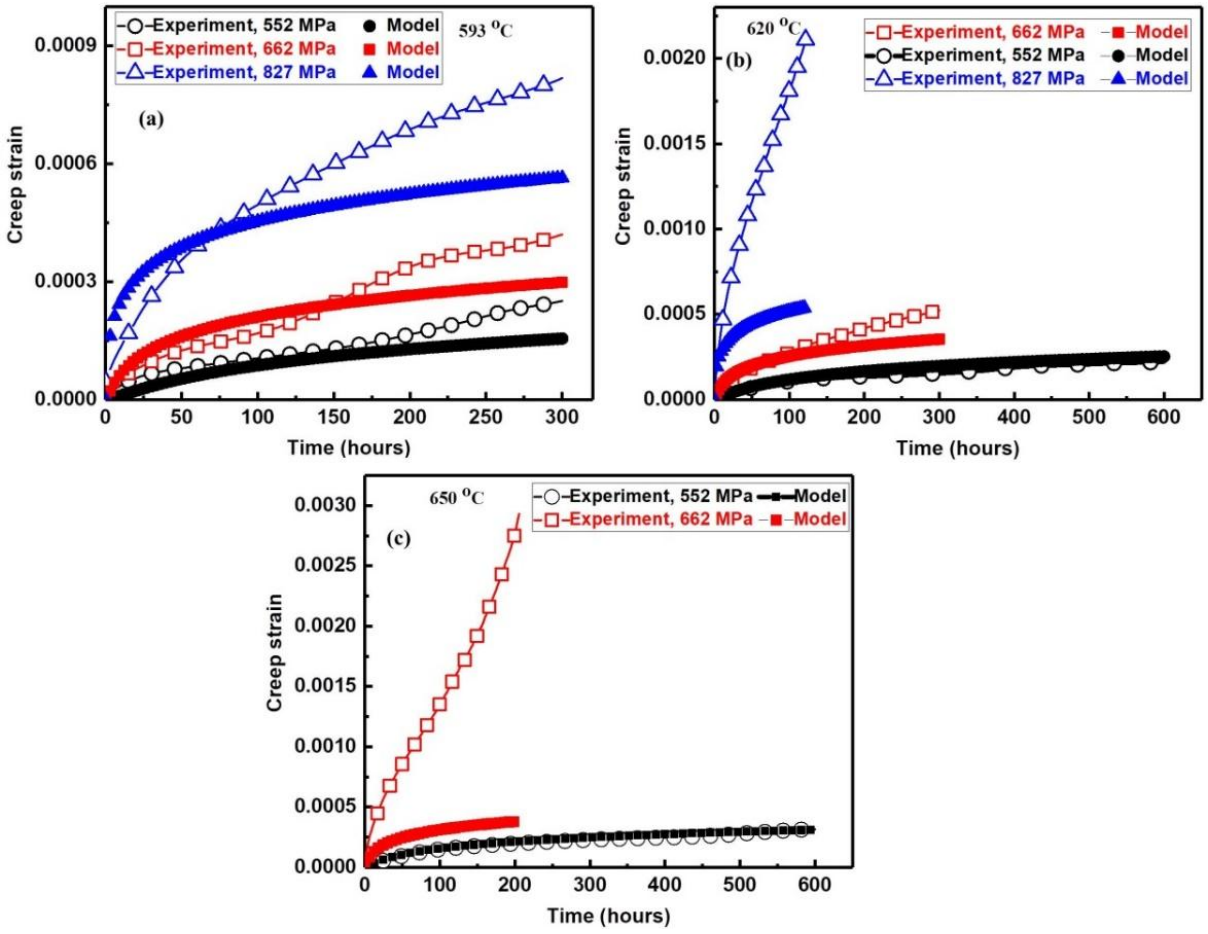

Figure 5.3. Simulated vs. experimental creep curves of IN-718 superalloy at (a) 593 ℃ / 552 MPa, 662 MPa, and 827 MPa; (b) 620 ℃ / 552 MPa, 662 MPa, and 827 MPa; (c) 650 ℃ / 552 MPa and 662 MPa

It has to be mentioned that the model does not consider cavitation the dynamic recrystallization occurred during creep. This could be the reason that limits the model capability to address the tertiary creep and deviation from experimental data for higher stresses. It can be observed that at constant *T*, higher stress leads to a higher creep rate and leading to accumulation of large creep strain, when compared to the same creep time (see Figure. 5.3a). It may be understood in a way that larger stress will lead to faster movement of dislocations resulting in more accumulation of creep strain. Similarly, at constant stress, observation is concomitant and higher *T* stimulates the accumulation of large creep strain due to the enhanced movement of dislocations at elevated temperatures [139].

The experimental creep curve shows a slight change in the creep rate after approximately 150 hours. It is more possibility that DRX is triggered in the secondary creep regime, likely due to the increased dislocation density at higher stress, which results from the high operational frequency of the Frank-Read source. This leads to the accumulation of high stored energy, thereby favoring the nucleation and growth of DRX grains. Furthermore, the activation of DRX triggers this increase in the creep rate as reported in the literature for the another nickel based super alloy CM247LC [227].

5.5.2. *Substructure evolutions*

The model can also simulate the microstructure evolution such as ρ_m and ρ_i. Figures 5.4a, b and c show the evolution of ρ_m and Figures 5.5a, b and c show the evolution of ρ_i at the different creep exposure conditions. Both dislocation densities evolved fast at the beginning of creep and saturates when reaching larger strains.

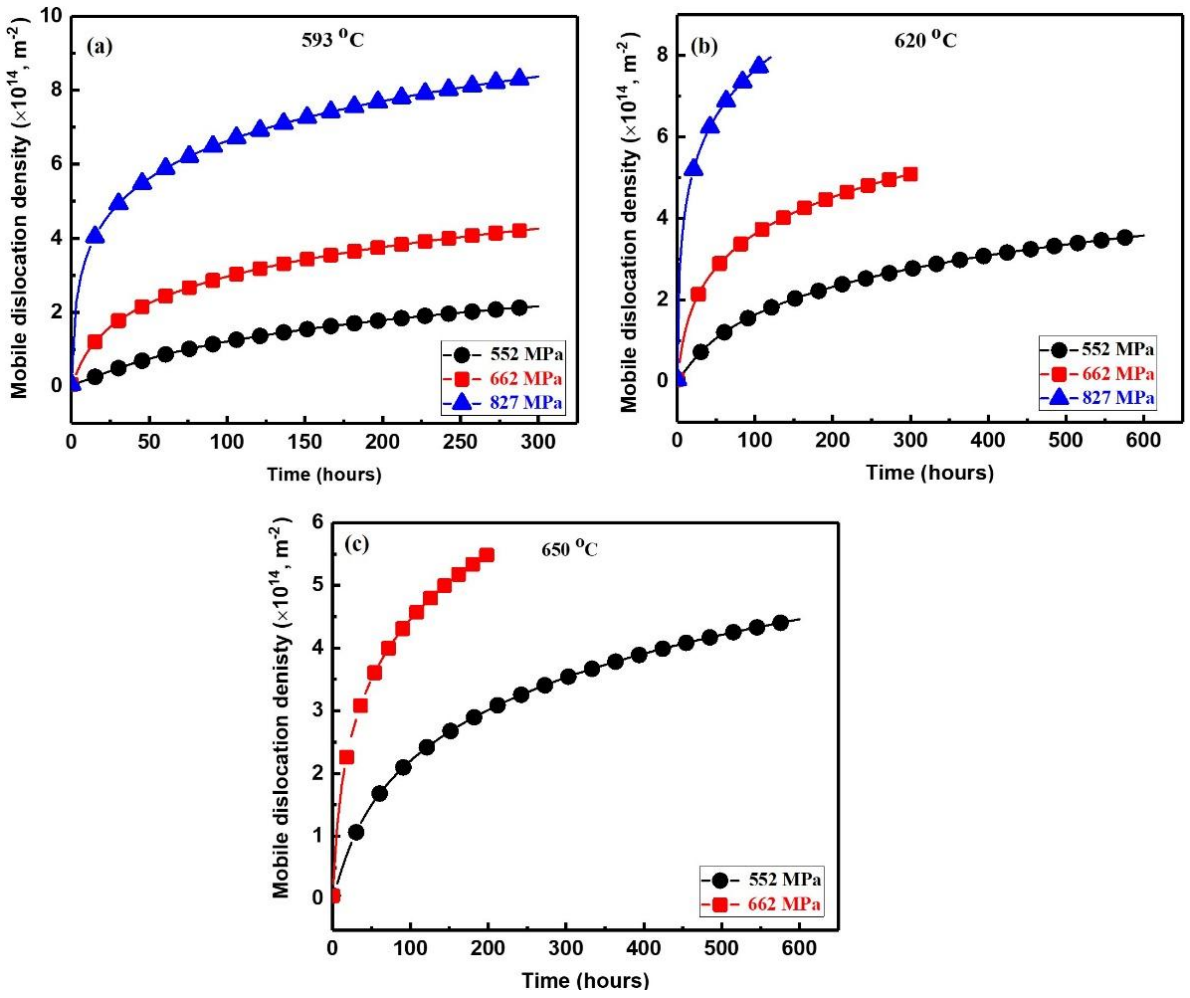

Figure 5.4. Predicted ρ_m vs. time of IN 718 superalloy at (a) 593 ℃ / 552, 662 and 827 MPa, (b) 620 ℃ / 552, 662 and 827 MPa, (c) 650 ℃ / 552 and 662 MPa

At the beginning of the creep, the production rate of the dislocations is high due to the operation of the F-R source mechanism at a higher frequency. As a result, it increases the dislocation density, hardens the material, and primarily decreases the strain rate during the primary creep stage. After the progression of the primary creep, the operation frequency of the F-R sources is supposed to be retarded due to the presence of more obstacles that are newly formed dislocations, leading to a decrease in the strain rate.

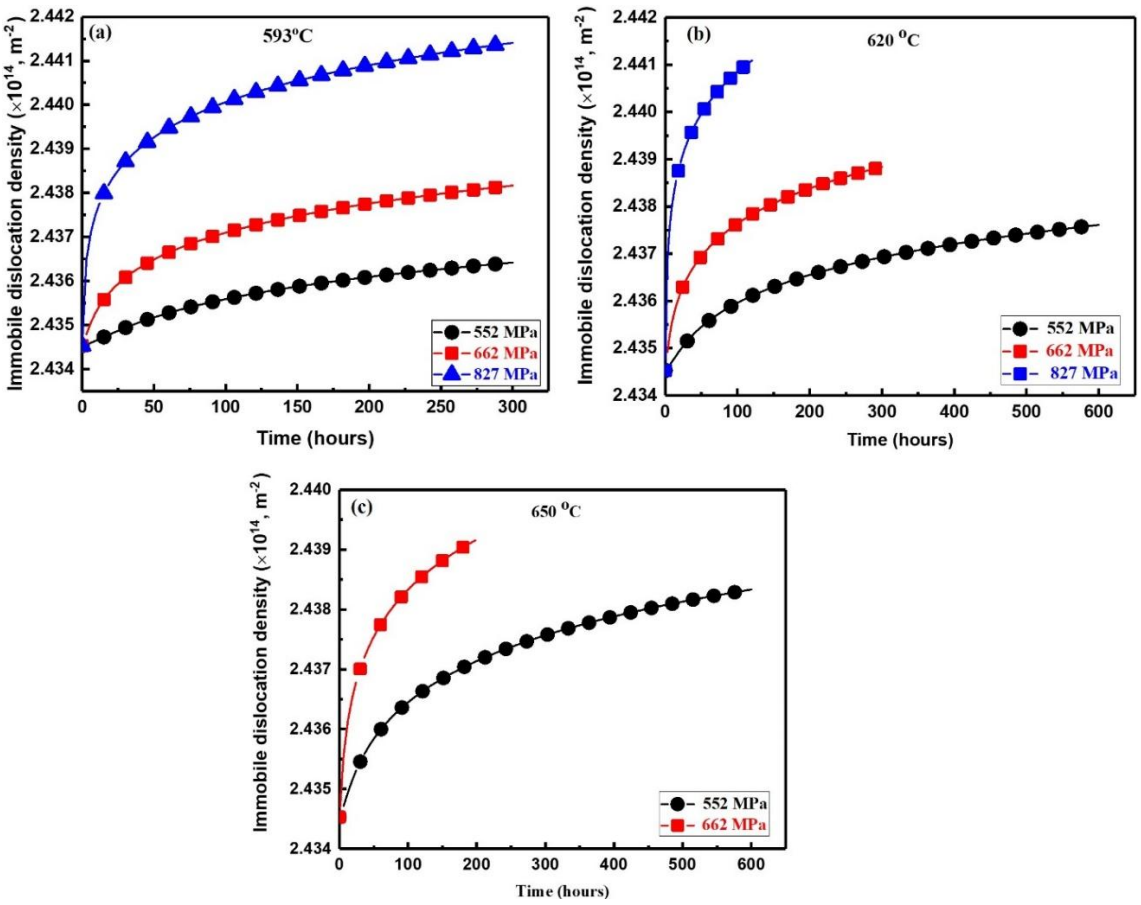

Figure 5.5. The evolution ρ_i of IN-718 superalloy at (a) 593 ℃ / 552, 662, and 827 MPa (b) 620 ℃ / 552, 662, and 827 MPa (c) 650 ℃ / 552 and 662 MPa

The model predicts a higher amount of dislocations at higher stress levels due to the Frank-Read source mechanism, similar to the work of [41, 139]. The model output such as ρ_m and ρ_i lies in the range of $2.17 \times 10^{14.0} - 8.37 \times 10^{14.0}$ m^{-2} and $2.42 \times 10^{14.0} - 2.45 \times 10^{14.0}$ m^{-2}, respectively, for the explored exposure conditions. Some other dislocation density data related to the creep of Ni-base alloys collected from the literature is given in Table 5.5. It can be deduced the alloy type and the conditions of the deformation play a major role in determining the magnitude of both types of dislocation densities. However, the prediction of dislocation densities from this model is concomitant to the literature with respect to the order of magnitude.

Table 5.5. Dislocation density reported in the literature for Ni-based superalloys after different creep conditions

Material	**ρ, m^{-2}**	**Conditions**	**Reference**
Ni- single crystal	$10.0 \times 10^{13.0}$	850 ℃ / 500 MPa	[204]
Ni-based superalloy	$1.6 \times 10^{14.0}$	900 ℃ / 450 MPa	[228]
Haynes 282	$1.5\text{-}18.0 \times 10^{13}$	760 ℃ / 190-310 MPa	[139]
Superalloy 617	$7.8\text{-}99.0 \times 10^{13.0}$	700 ℃ /165-200 MPa	[229]

5.5.3. *Evolution of mean free path*

The mean free path (λ_{mean}) is related to the density of dislocations, substructure size and the precipitates, see Equation 5.3. Figures 5.6a, b and c show the evolution of λ_{mean} for the different creep exposure conditions

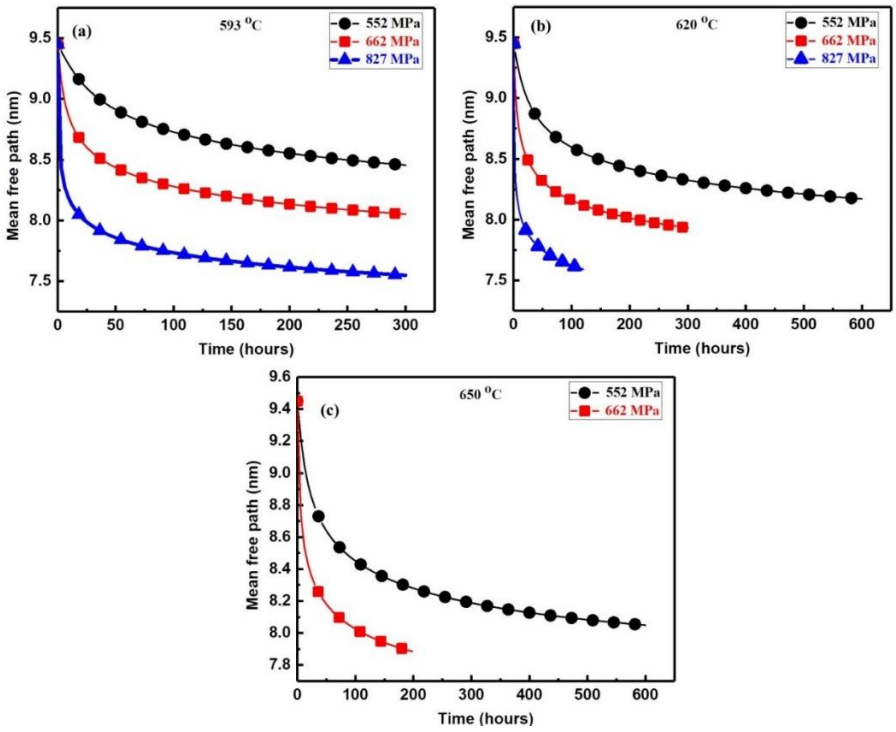

Figure 5.6. The evolution of λ_{mean} for IN-718 superalloy at (a) 593 ℃ / 552 MPa, 662 MPa and 827 MPa; (b) 620 ℃ / 552 MPa, 662 MPa and 827 MPa; (c) 650 ℃ / 552 MPa, and 662 MPa

. The λ_{mean} decreases very fast during the beginning of the creep because many dislocations are produced (mobile and immobile).As the creep time progresses, the λ_{mean} decreases at a relatively slow rate. Also, the higher the applied stresses σ_{appl}, the faster the obstacle mean path λ_{mean} decreases. As observed from Equation (5.3), the mean obstacle spacing consists of different contributions from the microstructure, such as the average distance between the mobile dislocations, the dislocations at cell boundaries and the various precipitates. Figures 5.7 show the evolution of these contributions for the creep condition 593 ℃ / 552 MPa. It can be observed that the precipitate provides the shortest obstacle spacing among all the other ingredients and dominates while deciding the order of magnitude of mean obstacle spacing.

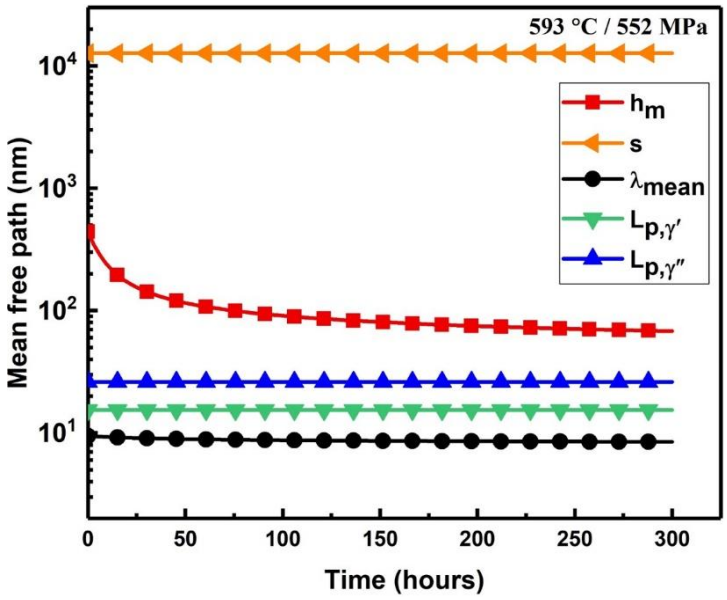

Figure 5.7. The evolution of h_m, s, $L_{p,}\gamma'$, $L_{p,}\ \gamma''$ *and* λ_{mean} for IN-718 superalloy at 593 ℃ / 552 Mpa

5.5.4. *Evolution of internal stress, effective stress, climb stress and glide velocity*

The evolution of $\sigma_{int,}$ $\sigma_{effe,}$ and σ_{cl} is depicted in Figure 5.8 for 620 ℃ / 552 MPa. It can be observed that the σ_{int} is increasing very fast at the beginning of the creep. It is reported that the heterogeneous

distribution of the dislocations (mobile and immobile) always leads to a significant amount of long-range internal stresses. At the beginning of the creep, it was observed that the magnitude of density of both dislocations increases and thereafter attain saturation and thus internal stress follows the same trend. At the end of the simulation magnitude of σ_{int} is predicted to be 432.13 MPa for 620 ℃ / 552 MPa. In the literature [230], σ_{int} is considered to be 10 % or more of the σ_{appl} and it was predicted close to 78 MPa for α iron at 400 ℃ / 196 MPa. In the case of P9 steel, the σ_{int} was observed to be in the range of 56-114 MPa at 600 ºC / 63-150 MPa [180].

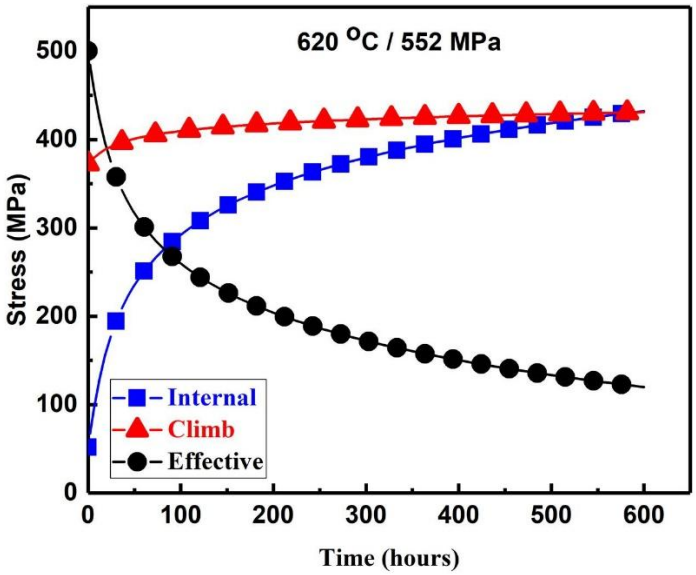

Figure 5.8. Predicted $\sigma_{int,}$ σ_{effe} and σ_{cl} vs. time curves of IN-718 superalloy at 620 ℃ / 552 MPa

In contrast to internal stress, the effective stress was observed to be decreasing with creep. It decreases very fast at the beginning of the creep and, thereafter, attains saturation. σ_{effe} is the stress available for the dislocation glide and it can be estimated by taking the difference between the σ_{appl} and the internal stress, see Equation. (5.8). It follows the opposite trend of σ_{int} in the beginning and thereafter saturates as the σ_{appl} remains constant. The magnitude of effective stress was predicted to be 119.86 MPa at the end of the simulation for the creep condition of 620 ℃ / 552 MPa. For the high SFE material like P9 steel, σ_{effe} was in the range of ~5-35 MPa at 600 ºC / 63-150 MPa. In

another study on P9 steel [179] σ_{effe} was predicted to be 5 MPa at 600 ºC / 80 MPa. In the case of P92 steel, the σ_{effe} was predicted in the range of ~ 134-149 MPa at the creep conditions of 600 ℃ / 145-160 MPa [58]. The magnitudes of the predicted σ_{effe} herein are found to be of a similar range reported in the literature and the deviation is due to different stresses, temperatures and composition.

Furthermore, it can be observed that the climb stress increases at the beginning of the creep and ends with a trend of saturation. At the beginning of creep, the resistance to the climb motion of the dislocation is lower due to a smaller number of obstacles, and thereafter the resistance increases due to overpopulation and so the climb stress increases. The magnitude of the climb stress is predicted to be 430.83 MPa for 620 ℃ / 552 MPa, at the end of the simulation. It is reported that the climb motion is easier at relatively higher σ_{appl} as it facilitates to overcome obstacles [139]. Climb stress was predicted for 9 Cr-1 Mo steel (without Nb, V and with Nb, V) and the magnitude lies in the range of 3.2 - 10.1 MPa, at 600 ℃ / 180 MPa [184] .

The evolution of v_{gl} is depicted in the Figures. 5.9a, b and c for the different creep exposure conditions. It is observed that the v_{gl} is decreasing very fast at the beginning of the creep and ends with a trend of saturation. Since dislocation production is high at the beginning of the creep, the overpopulation leads to a decrease in dislocation mobility. Furthermore, it is shown in Equation. (5.10), that the v_{gl} is directly concomitant with σ_{effe} hence, it follows the same trends as of the effective stress. The magnitude of v_{gl} was predicted in the range of $2.13\times 10^{-15.0}$ - 8.15×10^{-15} m/s at the end of the simulation, for the explored conditions. The influence of the stress at a constant temperature shows that the v_{gl} is higher for the lower σ_{appl} and vice-versa at the same rupture time. This can be understood in a way that, at low σ_{appl}, as the production of dislocations is low, thus an easy glide motion of the dislocation can be attained. Recently, the creep deformation and

microstructure investigation of 617 superalloys have been studied both experimentally and theoretically, and at 700 ℃ / 165-200 MPa, the magnitude of v_{gl} was reported to be in the range of $8.50 \times 10^{-15.0} - 5.70 \times 10^{-15.0}$ m/s [229].

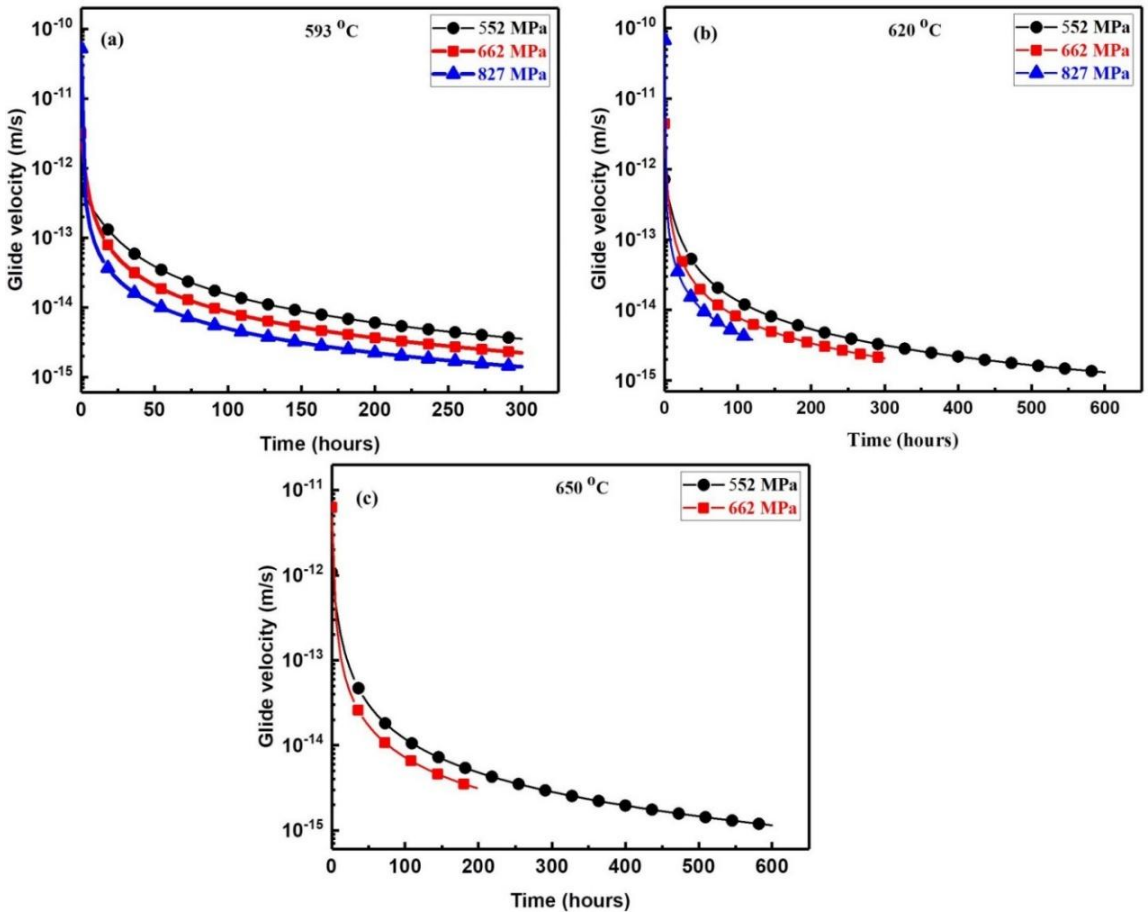

Figure 5.9. Predicted v_{gl} vs. time of a IN-718 superalloy at (a) 593 ℃ / 552-827 MPa, (b) 620 ℃ / 552-827 MPa, (c) 650 ℃ / 552-662 MPa

In the case of high SFE materials such as P91 steel, the average dislocation velocity is reported to be $2.0 \times 10^{-15.0}$ m/s for P91 steel at 600 ℃ / 80 MPa [174]. For another 9 %Cr steel, v_{gl} was predicted to be ~ $7.60 \times 10^{-13.0}$ m/s at 650 ℃ / 70 MPa [159]. Similarly, the stress dip test was conducted for the estimation of the v_{gl} in the case of pure Magnesium (Mg) as well as superalloy AS21 and the glide velocity was reported in the range of $1.0 \times 10^{-10.0} - 1.0 \times 10^{-4.0}$ m/s at 200-400

℃ / ~1-26 MPa [231]. The above discussion suggests that the v_{gl} strongly depends on materials and deformation conditions.

5.5.5. *Microstructure*

We analyzed the microstructures of as received and crept conditions employing EBSD. Figures 5.10a and b show the Inverse Pole Figure (IPF) overlapped with high angle grain boundaries (HAGBs), and Kernel Average Misorientation (KAM) maps for the as-received sample, respectively. The as-received microstructure consists of grains around 10 µm and annealing twins. The variation of color in the KAM map indicates the non-homogenous distribution of misorientation within regions with less than 5°. KAM map of as-received sample specimen is dominated by the presence of blue color depicting relatively lower KAM values and indicating lower magnitude of dislocation density.

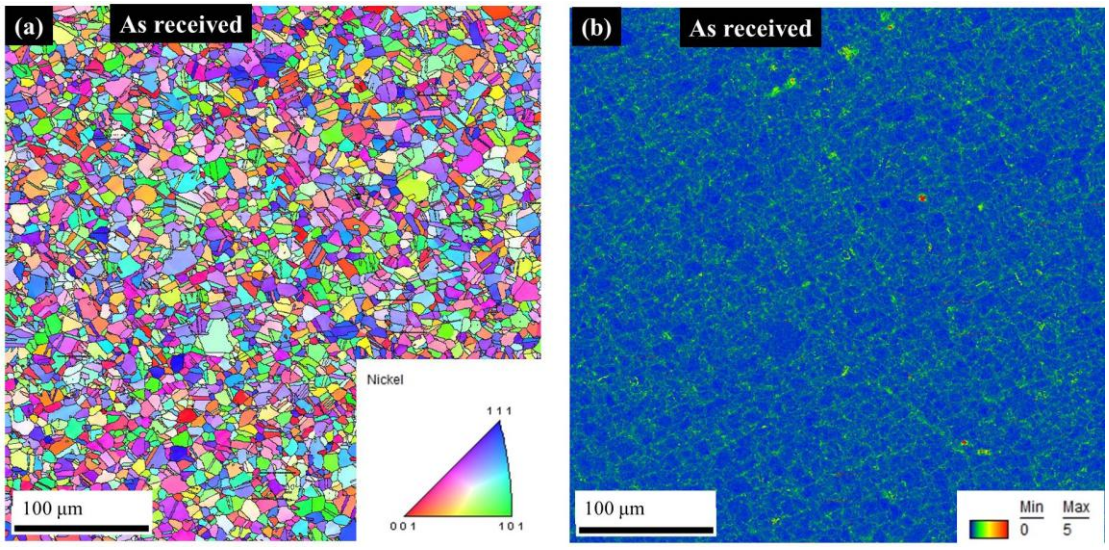

Figure 5.10. As received IN-718 superalloy (a) IPF Map and (b) KAM Map

Figures 5.11a and c depict the IPF map incorporating HAGBs in black color for the samples crept at 593 ºC / 662 MPa and 593 ºC / 827 MPa, respectively. Figures 5.11b and d depict the KAM map for the same samples. We observed that the local misorientation (KAM) is heterogeneously

distributed, with regions with high KAM values and areas with low KAM values. The higher KAM values (light green color) in the maps indicate that the material got hardened and lower KAM values indicates the local softening during creep. The KAM values are relatively higher for higher stresses and got enhanced during creep (see Fig. 2.11b and 2.11d).

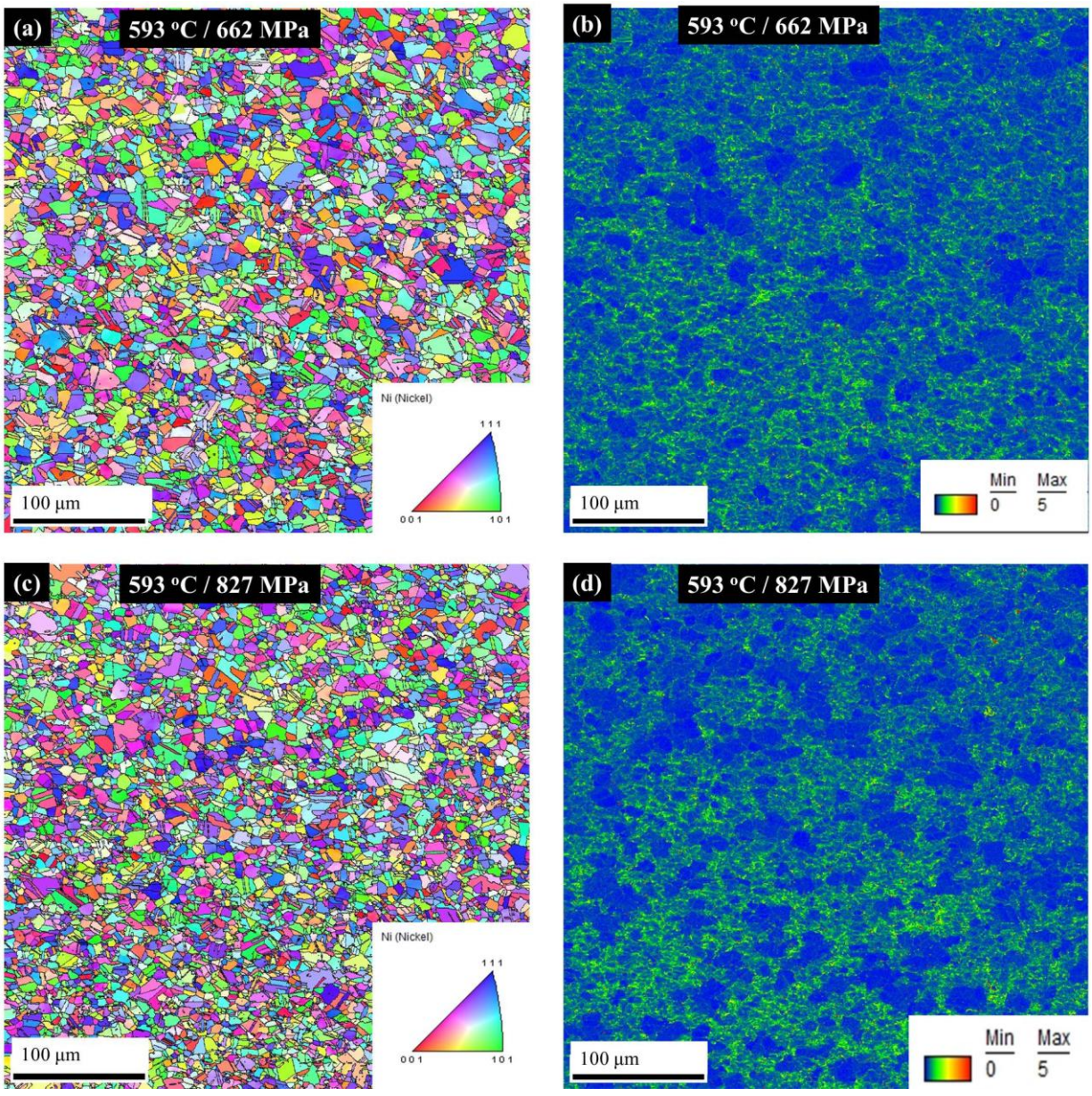

Figure 5.11. Crept IN-718 superalloy: IPF map and KAM map at 593 °C / 662 (a and b) and at 593 °C / 827 MPa (c and d)

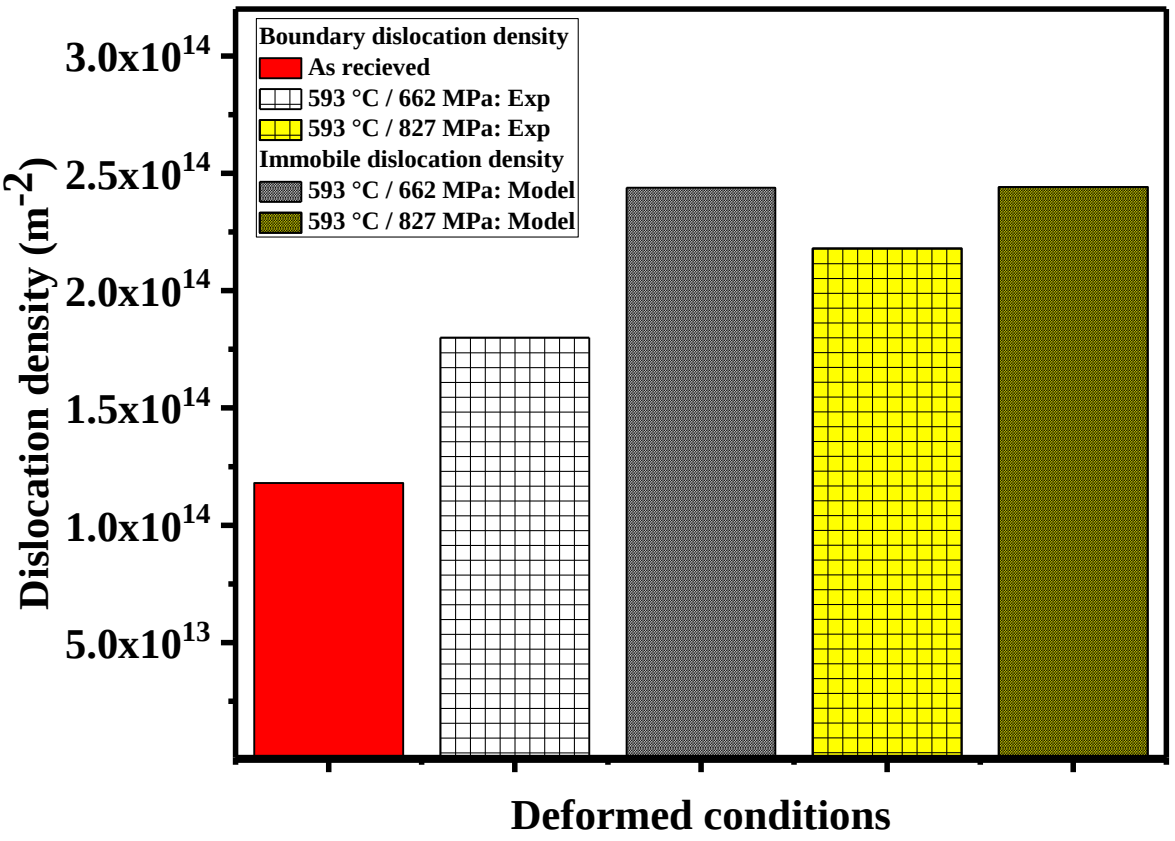

Figure 5.12. ρ_b from EBSD data and ρ_i from the model prediction for 593 ℃ / 662 and 593 ℃ / 827 MPa. ρ_b from EBSD data for as received.

To get more insights about microstructure evolution and hardening during creep, we estimated the boundary dislocation density (ρ_b) from EBSD data for as-received and crept conditions. The model for the estimation of ρ_b is adopted from Dronhofer et al. [232] which was also used in different work [98, 99, 220]. The aggregate ρ_b is estimated through the following expression,

$$\rho_b = \frac{\theta_i f_i}{2b} Z_{mean} \tag{5.14}$$

where, θ_i is the misorientation angle, f_i is the fraction of boundary, Z_{mean} is the ratio of surface area to volume and b is the Burgers vector equal to 2.54×10^{-10} m. The predicted internal variable ρ_i and

experimentally investigated ρ_b can be compared as they have some affinity [41], see Figure 5.12. Although ρ_i from the model and ρ_b from EBSD have some difference in magnitude, a similar trend that is, an increase in the magnitude with increasing stress at constant temperature, can be observed. It has to be mentioned that, our creep model only takes care of the hardened region, thus, the dislocation density from EBSD was estimated for the regions with high KAM values. The regions with lower KAM values where there is a possibility of dynamic recrystallization, were excluded while estimating the dislocation density.

5.6. Conclusions

In this work, a microstructure-based creep model has been developed and applied to understand the creep performance of the Inconel®718 superalloy. The creep tests were conducted and experimental creep curves were modelled and validated up to the secondary stage. In addition to this, the model was shown to be capable of addressing the evolution of the internal variables such as ρ_m, ρ_i, λ_{mean}, v_{gl}, σ_{int}, σ_{effe} and σ_{cl} with creep time. To get more confidence about the model predictions, the boundary dislocation density estimated from the EBSD characterization was compared with the dislocation density predicted by the model. From the explored conditions following conclusions can be drawn,

- The estimated magnitude of ρ_m and ρ_i, lies in the range of $2.17 \times 10^{14.0}$ - $8.37 \times 10^{14.0}$ m^{-2} and $2.42 \times 10^{14.0}$ - $2.45 \times 10^{14.0}$ m^{-2}, respectively.
- The magnitude of the λ_{mean} and v_{gl} lies in the range of 7.55-8.46 nm and $2.13\times 10^{-15.0}$ - 8.15×10^{-15} m/s.
- σ_{int}, σ_{effe} and σ_{cl} is predicted to be 432.13 MPa, 119.86 MPa and 430.83 MPa, respectively, for 620 °C / 552 MPa at the end of the creep.

- The model suggests that both the dislocation densities, internal stress and climb stress increase over the period of creep. Whereas the mean free path, glide velocity and effective stress have a decreasing trend.
- The proposed model is capable of addressing the effect of the stress and temperature on the primary to steady state creep regime using a single set of parameters.

Appendix 5.A

Estimation of stacking fault energy

SFE of the nickel-based superalloy is associated with temperature (T) and chemical composition (x), and it is described as [56],

$$SFE_{T,x} = SFE_{T,Ni}\left(1 + SFE_{x,\gamma}\right) \quad (5.A.1)$$

Where, SFE_T is the temperature-dependent SFE of pure Nickel and delineated as[233, 234],

$$SFE_{T,Ni} = 128.0 - 1.2240 \times 10^{-2.0} \times (\mathrm{T} - 300.0) - 3.4340 \times 10^{-6} \times (\mathrm{T} - 300.0)^2 \quad (5.A.2)$$

Herein, $SFE_{x,\gamma}$ is the chemical composition dependent SFE of pure γ matrix and delineated as [233],

$$SFE_{x,\gamma} = \sum_i x_i \delta SFE_i \quad (5.A.3)$$

where δSFE_i is represented as,

$$\delta SFE_i = \frac{1}{\Delta x_i}\left(\frac{\Delta SFE_i}{128}\right), \quad (5.A.4)$$

In A.4, Δx_i is a difference in the mole fraction of the super alloying elements, ΔSFE_i is the value of SFE for the individual alloying elements, associated with experimental data [235-238] for the nickel-based superalloys.

Appendix 5.B

Ostwald ripening constant

$$k_{d_1} = \left(k_{d_{\gamma',0}} e^{-\frac{30829.25}{T}}\right)/T \qquad (5.B.1)$$

$$k_{d_2} = \left(k_{d_{\gamma'',0}} e^{-\frac{45250}{T}}\right)/T \qquad (5.B.2)$$

where $k_{d_{\gamma',0}}$ and $k_{d_{\gamma'',0}}$ are coarsening constant and their values are $1.2910\times 10^{-16.0}$ and $1.8752\times 10^{-8.0}$, respectively.

Appendix 5.C

Diffusion coefficient

$$D_{vp} = 15 \times 10^{-4.0} \times 7.1710^{-6.0} \times e^{-Q_{vp}/RT} \qquad (5.C.1)$$

$$D_s = 9.2 \times 10^{-5.0} \times 0.017911093 \times e^{-Q_{sol}/RT} \qquad (5.C.2)$$